

Research Article

Numerical Analysis of Fracture Behaviour on Marble Samples Containing Two Flaws

Lifei Zheng , **Dan Huang** , **Xiaoqing Li**, and **Xuan Hu**

School of Civil Engineering and Mechanics, Huazhong University of Science and Technology, Wuhan 430074, China

Correspondence should be addressed to Dan Huang; 2017502016@hust.edu.cn

Received 29 August 2019; Revised 22 November 2019; Accepted 3 January 2020; Published 30 January 2020

Academic Editor: Yinshan Tang

Copyright © 2020 Lifei Zheng et al. This is an open access article distributed under the Creative Commons Attribution License, which permits unrestricted use, distribution, and reproduction in any medium, provided the original work is properly cited.

Uniaxial compression tests were conducted on marble specimens containing two flaws. There are coplanar flaws and noncoplanar flaws. The inclination angle and spacing of flaws were considered of the coplanar flaws model, and the step angle and spacing of flaws were considered of the noncoplanar flaws model. Strength failure and crack coalescence behaviour were analysed in the paper. The crack evolution process containing microcrack initiation, coalescence, and failure is focused on the rock bridge coalescence and the extent of the pre-existing flaws. There are four forms of rock bridge coalescence: tensile crack coalescence, shear crack coalescence, mixed tensile and shear crack coalescence, and no coalescence. Also, there are four forms of the rock failure mode: tensile failure, shear failure, mixed tensile and shear failure, and split fracture. The outer end of the critical stress values were used to compare with the crack initiation strengths, and the crack initiation strengths were slightly larger than the critical stress. In addition, energy dissipation laws were analysed during the model fracturing process. The crack evolution mechanisms around the pre-existing flaw in the model were revealed by the distribution of microcrack and energy dissipation.

1. Introduction

With the rapid development of civil and traffic engineering and the exhaustion of shallow resources and energy, many rock projects have entered deep environment; therefore, crack evolution lead to frequent instability failure accidents of rock mass underground engineering. The Jinping II Hydropower Station is located on the main stream of the Yalong River in the Liangshan Yi Autonomous Prefecture in Sichuan Province and is one of the backbone hydropower stations developed by the lower reaches of the Yalong River. Marble is the main surrounding rock of the Jinping II Hydropower Station. The fracture evolution process of the crack in the rock mass is an urgent scientific problem to be solved in deep underground rock engineering. Therefore, we consider the pre-existing flaws in the model, and fracture mechanics and crack coalescence behaviour of the marble containing pre-existing flaws are researched.

To better understand fundamental cracking processes, precracked samples under compression have been extensively studied in experiments on different natural rocks [10, 11, 20–22] and rock-like materials [2, 16–18].

The experimental study is based on the rocks with natural flaws and rock-like materials with man-made pre-existing flaws. In addition to physical experimental studies, numerical simulation also plays a major role in crack coalescence research. Over the last two decades, the discrete element method (DEM) has emerged as a powerful tool for exploring the mechanical behaviour of intact and jointed rock masses at both the laboratory field scales [1, 8]. DEM numerical investigations are carried out for several rock materials containing different fissure geometries, such as a single flaw, two flaws, and three flaws [25–28]. Recently, the synthetic rock mass (SRM) approach has been employed for a more realistic simulation of jointed rock masses [12]. In this approach, intact rock is represented by Bonded Particle Model (BPM), which has been extensively used for rock failure analyses over the past decade [3, 14]. The pre-existing flaws are represented by SJM, which simulates the behaviour of a smooth interface created by a joint plane and reflects the predominant influence of joint orientation and inclination on the joint, and hence, the whole rock mass behaviour, by neglecting the local particle contact geometry surrounding the joint plane [15]. The author has proposed a detailed study

on the capabilities and limitations of SJM for producing realistic rock behaviour, particularly for the effects of the various microparameters of the model on simulated macroproperties and the associated failure modes of rock masses [5].

Crack coalescence of the two flaws and the rock bridge coalescence model was important for the cracking processes in the rock mass. Bobet and Einstein [2] proposed five coalescence categories in a uniaxial compressive test and two additional coalescence categories in a biaxial compressive test. Sagong and Bobet [18] classified crack types into tensile cracks, quasicoplanar shear cracks, and oblique shear cracks. Wong [24] did the gypsum and marble specimens for the one or two flaws and summarized the coalescence behavior. Nine coalescence categories were classified by Wong and Einstein [20] based on the various combinations of these cracks. The classification of coalescence mode on the DEM was based on the morphology of crack development at the failure stage or on the lab test based on the real time of photographic monitoring on the model surface. The advantage of this paper is combining the DEM simulation and fracture mechanics to analyse the cracking process.

Based on the DEM, the stress distribution status of the model in the process of loading at a different stage can be used to validate the real-time cracking evolution analysis. The author has proposed this method and describes it in detail in the article [5]. In addition to determining the crack initiation stress and crack damage stress, peak strength based on numerical calculation, the stress intensity factor, outer side critical stress, and internal side critical of flaws based on the fracture mechanics were used in this article. The analytical solutions of coplanar flaws were given by Erdogan [7]; interaction between flaws and the stress intensity factor at outer and internal tips of flaws was listed. Fracture energy was an important aspect to observe the cracking process [25, 30]; thus, the fracture energy was used to analyse the law of energy change during the samples loading.

Crack coalescence behaviour and fracture mechanics analysis are the research objective of this paper. Intact rock specimen and rock specimen containing two flaws are constructed, the strength and crack evolution behaviour are discussed, the stress redistribution is used to analyze rock bridge coalescence behaviour, and the rock bridge coalescence mode and rock failure mode are summarised. The critical stress based on the fracture mechanics was obtained, and fracture energy analysis was studied in this article.

2. Model Construction

2.1. Intact Rock Specimen and Microparameters. In this research, particle flow code (PFC) based on DEM, was used to simulate the mechanical behaviour of the marble specimens containing pre-existing flaws under uniaxial compression. The BPM has a demonstrated ability to reproduce many features of rock behaviour, including elasticity, fracturing, acoustic emission, damage accumulation that produces

material anisotropy, hysteresis, dilation, postpeak softening, and strength increase with confinement, which can be found in [9, 13, 14]. The generation of BPM is roughly divided into the following five steps as shown in Figure 1. As a result, the flaws are created by the smooth-joint model, which provides the macroscopic behaviour of a linear elastic and either bonded or frictional interface with dilation.

A 50 mm × 100 mm rectangular numerical model was constructed, which was of the same scale as the experimental marble specimen. The particle sizes distribution of the model was from 2.0 mm to 3.32 mm. The BPM was constructed and calibrated against the laboratory test results from the marble samples extracted from the Jinping II hydropower station site located at the Yalong River of Sichuan, see [4]. The model is calibrated by the “trial and error method.” Mesoscopic numerical simulation makes the macroscopic mechanical response of the model close to the actual material by changing the mesoscopic parameters of the particle and interparticle contact model. In the whole process, approximating the elastic modulus of rock by changing the elastic modulus of the particle and the elastic modulus of the parallel bond, the two are positively correlated; changing the particle stiffness ratio and the parallel bond stiffness ratio to obtain a similar Poisson’s ratio, which is a positive correlation and changing the parallel bond normal strengths and tangential strengths to approximate the peak intensity, the two are positively correlated.

Table 1 lists the microparameters for the marble specimen used in the PFC^{2D} modelling. Table 2 lists the laboratory measurements and model predictions of macroproperties of Jinping marble.

Figure 2 shows the comparison of the stress-strain curves and ultimate failure modes obtained from the experiment and PFC^{2D} simulation. As seen in Figure 2, the DEM method can accurately reflect the mechanical properties of rock in the compression test; the numerical curve reproduced the elastic deformation, peak strength, nonlinear deformation, and brittle failure of the experiment, but did not reproduce the initial deformation stage. In addition, the numerical model produced a splitting failure mode, which was also similar to the experimental result.

2.2. Rock Specimen Containing Two Flaws. The sketch of rock containing two flaws and the numerical model containing one flaw is shown in Figure 3. The model is in a 50 mm × 100 mm rectangular numerical mode, and two pre-existing flaws are represented by the inclination angle α (same as dip angle), stepped angle β , spacing D , and the flaw length L . The particle is represented by the yellow ball, the flaw plane is represented by the blue disk, and the smooth joint contact is represented by the black disk. The microparameter properties of the smooth joint model are listed in Table 3. The uniaxial compression test was taken for the sample with two flaws. The micro-parameter geometries of the test are listed in Table 4. There are five series of the uniaxial compression test: series 1 and 2 are coplanar two flaws and series 3, 4, and 5 are noncoplanar two flaws.

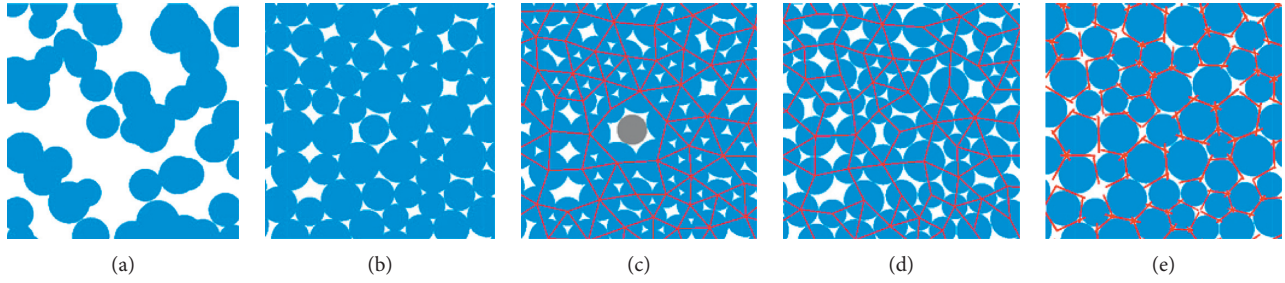


FIGURE 1: Generation steps of BPM. (a) Randomly generated, (b) particle balance, (c) floater particle, (d) contact well, and (e) parallel bond.

TABLE 1: The microparameters of the BPM numerical model.

| Particle parameters | | Parallel bond parameters | |
|---------------------|------|--------------------------|----------------|
| E_c (GPa) | 35 | \bar{E}_c (GPa) | 35 |
| k_s/k_n | 0.4 | \bar{k}_n/\bar{k}_s | 0.4 |
| μ | 0.5 | $\bar{\sigma}_c$ (MPa) | 124 ± 24.8 |
| R_{\max}/R_{\min} | 1.66 | $\bar{\tau}_c$ (MPa) | 124 ± 24.8 |
| R_{\min} (mm) | 1 | $\bar{\lambda}$ | 1.0 |

TABLE 2: Laboratory measurements and model predictions of macroproperties of Jinping marble.

| Macroproperties | R_c (MPa) | E (GPa) | ν (%) |
|------------------------|-------------|-----------|-----------|
| Laboratory measurement | 140 | 31.6 | 0.24 |
| Model prediction | 136.8 | 33.1 | 0.22 |

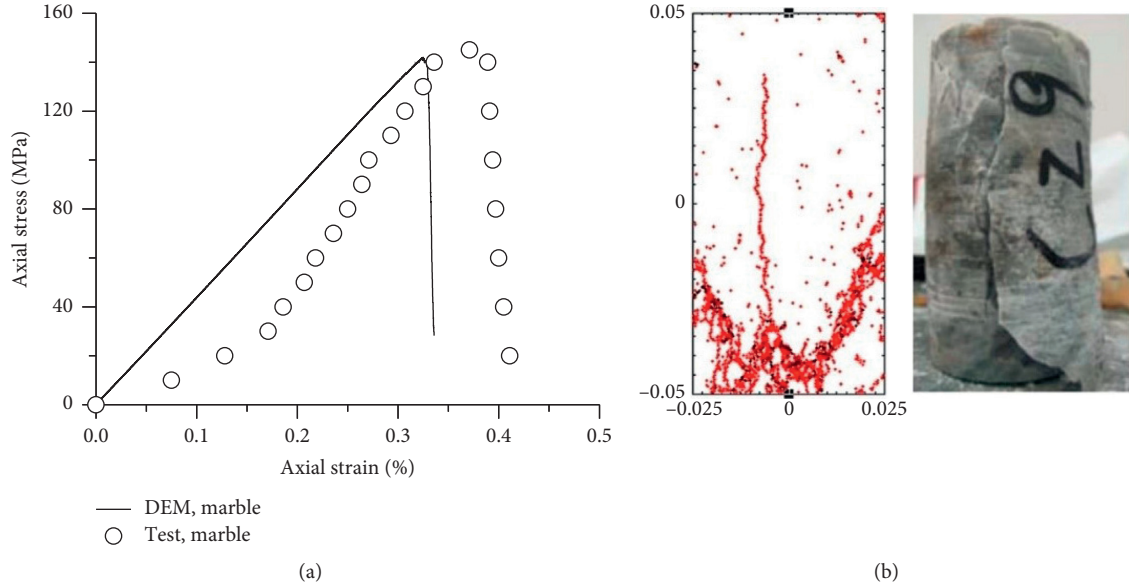


FIGURE 2: (a) Axial stress-stain curves and (b) failure mode [4].

3. Strength and Crack Evolution Behaviour

3.1. Peak Strength. Figure 4(a) shows the relationship between the peak strength and flaw inclination angle of the specimens containing coplanar flaws of the model series 1, and Figure 4(b) show the relationship between the peak strength and flaw spacing of the specimens containing coplanar flaws of the model series 2. As seen in Figure 4(a), the

peak strength increases with the increase in the flaw inclination angle, the sample containing the inclination angle α of 75° and 90° has the higher peak strength. As seen in Figure 4(b), the peak strength has very little change with increases of the flaw spacing. The sample containing the spacing L of 10 mm has the highest peak strength.

Figure 5 shows the relationship between step angle β and peak strength of the model with noncoplanar flaws of the

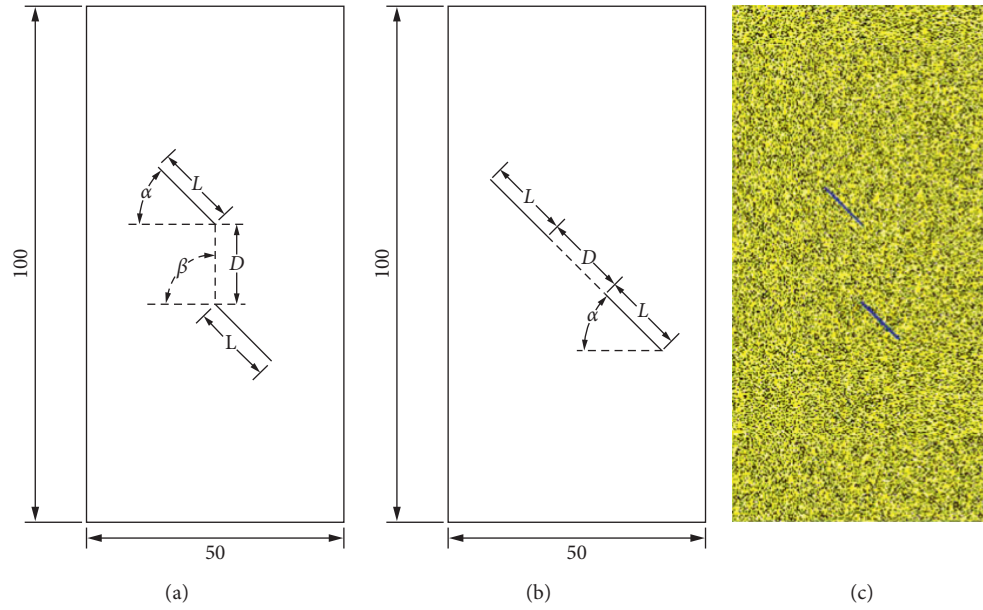


FIGURE 3: (a) Sketch of rock containing noncoplanar two flaws; (b) sketch of rock containing coplanar two flaws; and (c) rock model containing two flaws.

TABLE 3: The properties microparameters of the smooth joint model.

| k_n (GPa) | k_s (GPa) | σ_j (MPa) | τ_j (MPa) | μ | Φ (°) |
|-------------|-------------|------------------|----------------|-------|------------|
| 2.0 | 2.0 | 0 | 0 | 0.5 | 35 |

TABLE 4: The microparameter geometries of the two flaws in the test.

| | Relationship | Inclination angle α (°) | Stepped angle β (°) | Spacing D (mm) | Flaw length L (mm) |
|----------|--------------|--------------------------------|----------------------------|-------------------|----------------------|
| Series 1 | Coplanar | 0, 15, 30, 45, 60, 75, 90 | 45 | 10 | 10 |
| Series 2 | Coplanar | 45 | 45 | 5, 10, 15, 20, 30 | 10 |
| Series 3 | Noncoplanar | 45 | 0, 15, 30, 45, 60, 90, 120 | 10 | 10 |
| Series 4 | Noncoplanar | 45 | 0, 15, 30, 45, 60, 90, 120 | 15 | 10 |
| Series 5 | Noncoplanar | 45 | 0, 15, 30, 45, 60, 90, 120 | 20 | 10 |

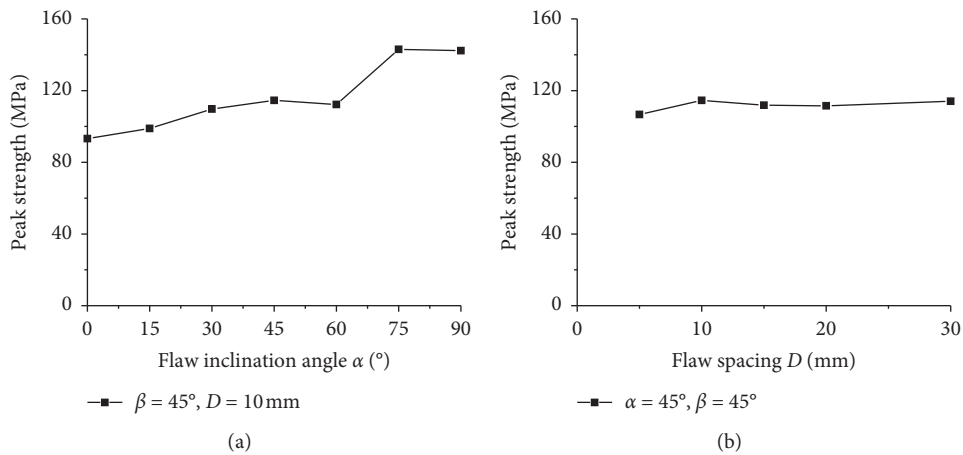


FIGURE 4: (a) The relationship between flaw inclination angle and peak strength and (b) the relationship between flaw spacing and peak strength.

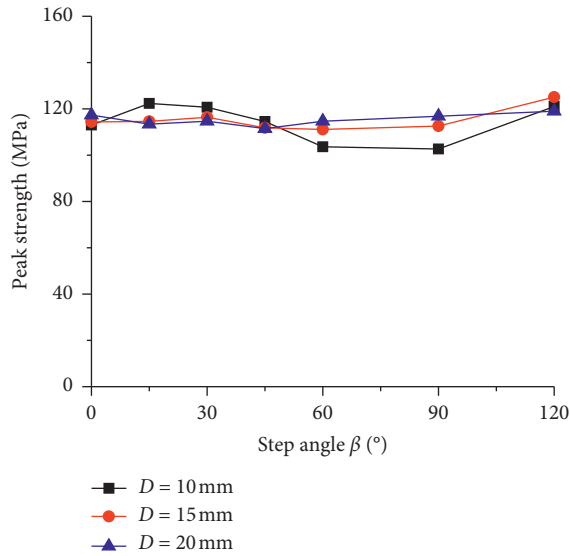


FIGURE 5: The relationship between step angle and peak strength of the model with noncoplanar flaws.

model series 3, 4, and 5. It can be seen that the peak strength has very little change with the increases in the step angle.

3.2. Crack Initiation Stress and Crack Damage Stress. The crack initiation stress and crack damage stress were obtained from the numerical simulation. The crack initiation stress is defined as the axial stress that initiated the first cracks in the preflaw samples, and the crack damage stress is defined as the axial stress when the crack begins to grow unsteadily in the preflaw samples. The crack damage stress is defined based upon the shape of the microcrack. Two methods of microcrack fitting and microcrack azimuth principal component analysis are used to judge the penetration condition of microcracks observed during the uniaxial compression test, and the damage of the sample was determined when the rough surface was formed. The author had used this approach to analyze the crack initiation stress and the crack damage stress in the intact marble samples [6].

Figure 6 presents the characteristic stress ratio of marble specimen containing coplanar two flaws under the uniaxial compression test. As seen in Figure 6(a), with the increase in the flaw inclination angle, the ratio of the crack initiation stress to peak strength ranged from 0.5 to 0.7, and the ratio of the crack damage stress to peak strength ranged from 0.8 to 0.9. As seen in Figure 6(b), with the increase in flaw spacing, the ratio of the crack initiation stress to peak strength ranged from 0.45 to 0.55, and the ratio of crack damage stress to peak strength is about 0.9.

Figure 7 presents the characteristic stress ratio of the marble specimen containing noncoplanar two flaws under the uniaxial compression test. As seen in Figure 7, with the increase in the stepped angle, the ratio of the characteristic stress to peak strength has no big change. The ratio of the crack initiation stress to peak strength ranged from 0.4 to 0.6, and the ratio of the crack damage stress to peak strength range d from 0.7 to 0.95.

3.3. Fracture Evolution Behaviour. In order to research the rock stress distribution status in the process of loading, the model with coplanar flaws ($\alpha = 45^\circ$, $\beta = 0^\circ$, $D = 10$ mm, and $L = 10$ mm) is used as an example to understand the relationship between the stress redistribution and microcrack appearance. Figure 8 shows the microcrack distribution and axial stress contour at different stages, and the stress values, strain value, and number of microcracks (Ncm) were listed below the picture. Point *a* is located before the peak strength and the stress is 50.5 MPa. There is no microcrack, and the stress concentration area is the region between two cracks and the crack tip. Point *b* is located before the peak strength, and the stress reached to 76.8 MPa. The number of microcracks is 8, and the microcracks appear in the outer side of the tips. The stress concentration area is the region between two cracks and the crack tip, and the stress is increased. Point *c* is the close to the peak strength and the stress reaches to 156 MPa, the number of microcracks is 156, the microcracks appear in the inner side of the tips, and growth is observed in the outer tips. The stress concentration area is still the region between the two crevasses and the crack tip, and the stress value increases, indicating that the crack tip and rock bridge are more vulnerable to failure. Point *d* is located after the peak strength and close to the peak strength, and the number of microcracks is 632. The microcracks between the rock bridges are coalescence, and the microcracks at the outer tips are extended along the loading direction. The stress concentration area is still the region between the two crevasses and the crack tip. Point *e* is located after the peak strength. The stress is decreased to 73.2 MPa. The number of microcracks is 864, and the microcracks at the outer tips are continuing to grow along the loading direction. Because of the appearance of the microcracks, the stress concentration area is at the rock bridge and left and right side of the samples. Point *f* is located at the final failure. The stress is down to 22.8 MPa. The number of microcracks is 1275, the microcracks at the outer tips grow along the loading direction and reach to the top and bottom side of the sample, and the sample is broken. The stress in the rock is between 20 and 40, indicating that there is still a certain residual stress at the failure stage. In the process of stress redistribution in rock, the development of cracks can be roughly judged. The stress of the model decreases in areas where microcracks have appeared. The stress value of the model is the maximum in the area where the microcrack appears.

Figure 9 shows the microcrack evolution of the model with noncoplanar flaws and inclination angle of 45° rock bridge inclination angle of 90° spacing of 20 mm at different stages, and points *a*, *b*, *c*, and *d* are shown in the figure. Point *a* is before the peak strength, and several microcracks appear from the outer tips of two flaws. Point *b* is near the peak strength. The microcracks at the outer tips grow vertical to the flaws. Point *c* lies after the peak strength and near the peak strength, and the microcracks grow at the internal tips of flaws and a pair of microcracks grows along the loading direction at the outer tips of flaws. Point *d* is at the failure stage, the microcracks at the internal tips are coalescence, and the crack at the outer tips of the flaws grows to the top and the bottom of the model.

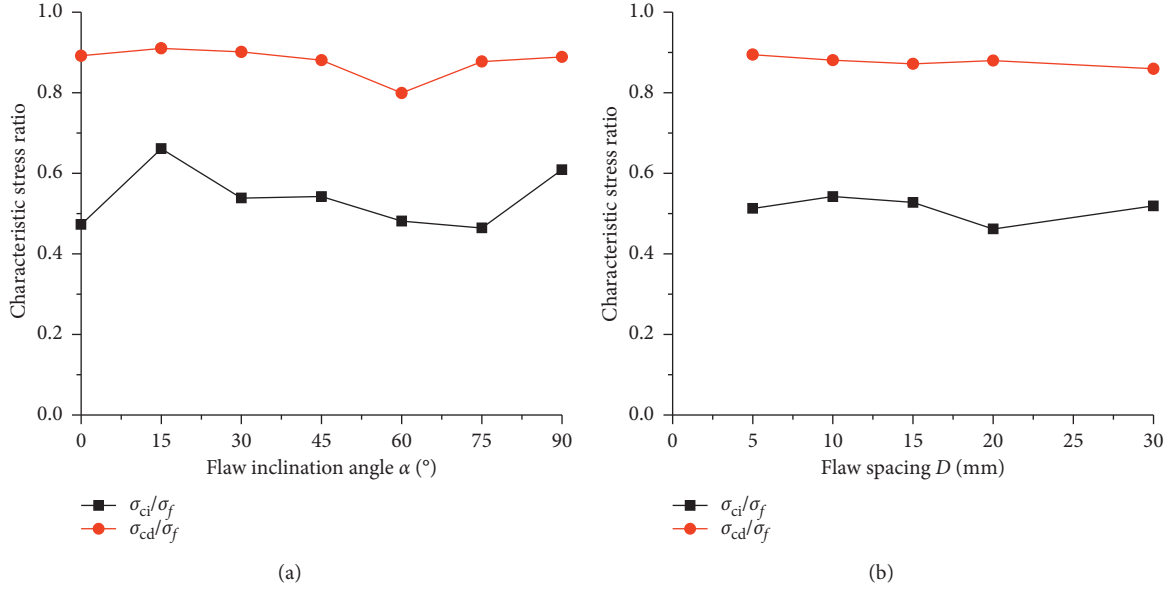


FIGURE 6: Characteristic stress ratio of the marble specimen containing coplanar two flaws. (a) Different flaw inclination angle and (b) different spacing.

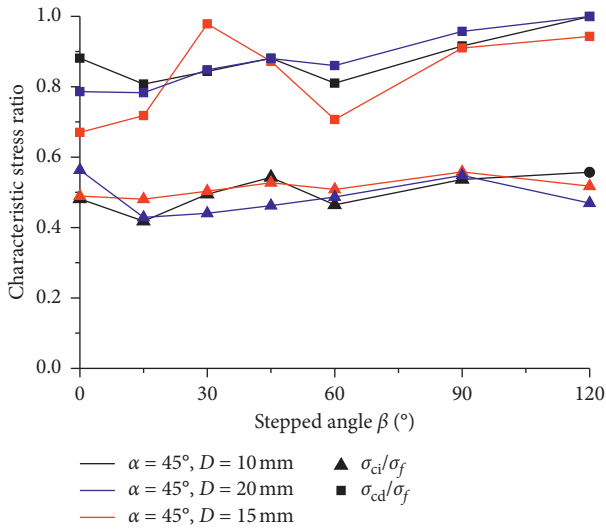


FIGURE 7: Characteristic stress ratio of marble specimen containing noncoplanar two flaws.

3.4. Rock Bridge Coalescences Mode and Rock Failure Mode. The microcrack distribution pictures of different models at the failure stage are selected, and the failure mode of the rock and the coalescences status of the rock bridge are classified as shown in Table 5. There are four forms of rock bridge coalescences: tensile crack coalescence; shear crack coalescence; mixed tensile and shear crack coalescence; and no coalescence. There are four forms of the rock failure mode: tensile failure; shear failure; mixed tensile and shear failure; and split failure.

3.5. Comparison with the Experiments and the Simulation. The comparison with the experiments and the simulation of a marble with two coplanar flaws is shown in Figure 10. The

experiment was conducted on Carrara marble specimens containing two coplanar flaws, the inclination angle of the marble was $0^\circ, 30^\circ, 45^\circ, 60^\circ$, and 75° , the length of flaw was about 13 mm, and the spacing of flaw was about 13 mm, which is similar to the simulation of this paper [24]. It can be seen that the failure mode of simulation was similar to the experiment. When the dip angle was 30° or 45° , the coalescence was achieved in an indirect manner by linkage of two pre-existing flaws, and the wing crack is appeared at the same time. When the dip angle was 60° , the coalescence was achieved in a direct manner by linking up directly with a continuous crack, and the wing crack is appeared at the same time.

4. Discussion

4.1. Fracture Mechanics Analysis. For the constant length coplanar flaw crack, the loading stress is p_1 . The far-field boundary condition for the crack under uniaxial pressure is

$$\begin{cases} \sigma_x^\infty = -p_1 \sin^2 a, \\ \sigma_y^\infty = -p_1 \cos^2 a, \\ \tau_{xy}^\infty = -p_1 \sin a \cos a. \end{cases} \quad (1)$$

The effect of σ_y^∞ on the model makes the crack surface close and generates positive pressure on each other, so there is $\sigma_N = \sigma_y^\infty$. When the flaw surface closes under pressure, the stress intensity factor at the crack tip $K_I = 0$. Friction exists on the closed flaws surface $\tau_f = f\sigma_N = f\sigma_y^\infty$. The boundary conditions of the flaw surface are $\tau_e = \tau_{xy}^\infty = \tau_{xy}^\infty - f\sigma_y^\infty$.

The stress intensity factor at the outer tip of flaw is

$$K_{II}(o) = \frac{\tau_e \sqrt{\pi} \cdot a^2}{\sqrt{a} \cdot \sqrt{a^2 - b^2}} \left[1 - \frac{E(k)}{K(k)} \right]. \quad (2)$$

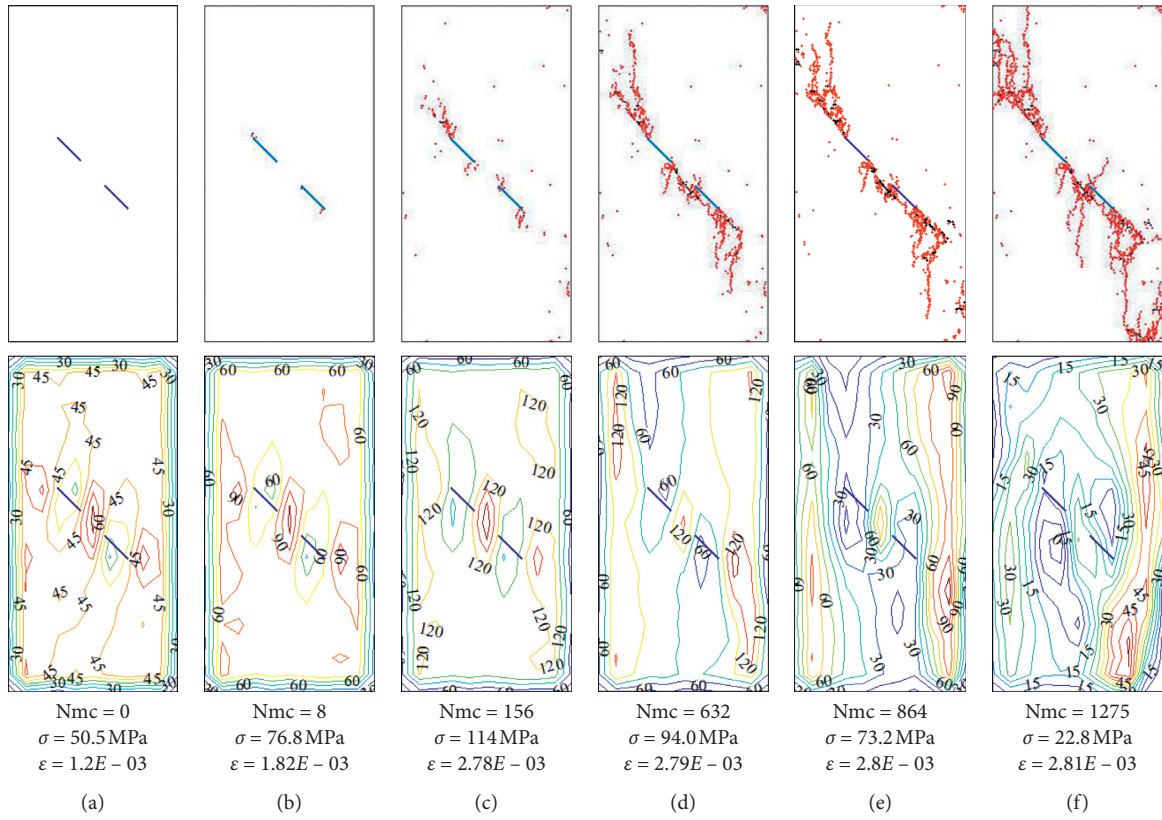


FIGURE 8: The microcrack distribution and axial stress contour at different stages.

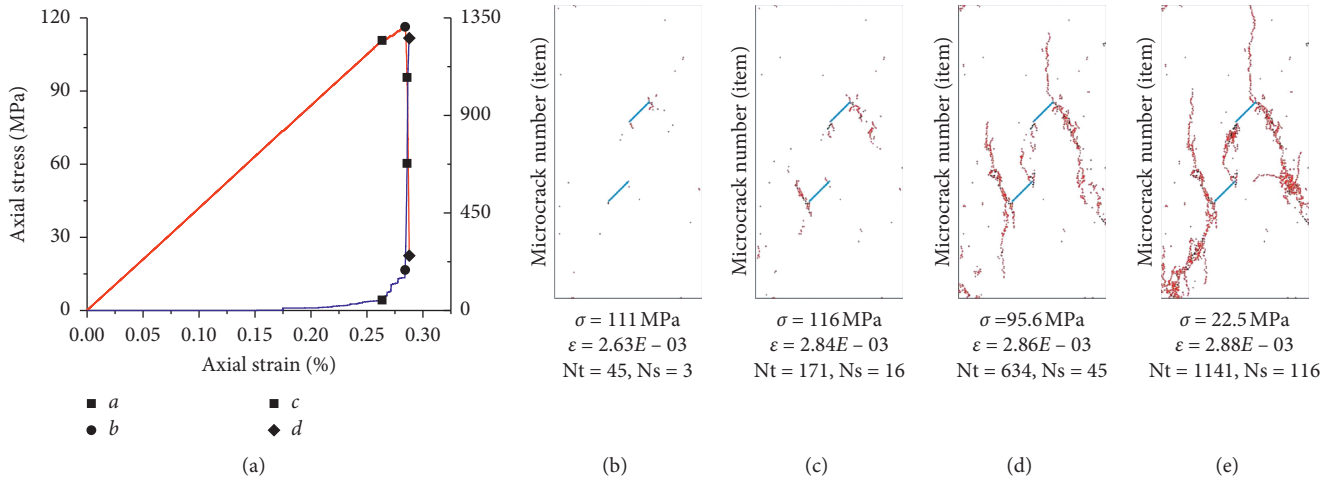


FIGURE 9: The microcrack evolution of the model with noncoplanar flaws ($\alpha = 45^\circ$, $\beta = 90^\circ$, $D = 20$ mm, $L = 10$ mm) at different stages.

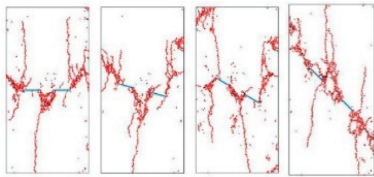
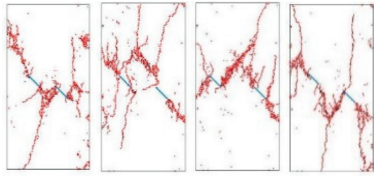
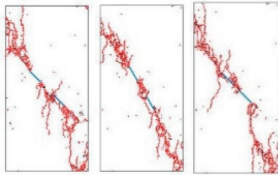
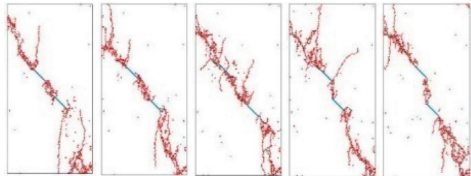
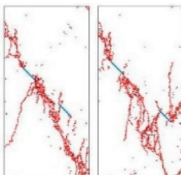
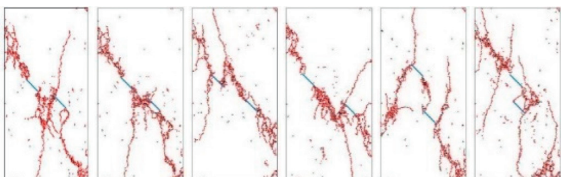
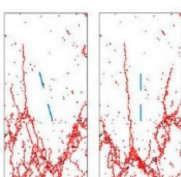
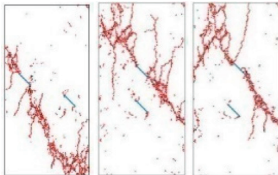
The critical stress at the outer tip of the flaw is

$$\sigma(o) = \frac{2K_{II}(o) \cdot \sqrt{a(a^2 - b^2)}}{(\sin 2\alpha + 2f \cos^2 \alpha)[1 - (E(k)/K(k))] \cdot \sqrt{\pi} \cdot a^2} \quad (3)$$

The stress intensity factor at the internal tip of the flaw is

$$K_{II}(i) = \frac{\tau_e \sqrt{\pi}}{\sqrt{b} \cdot \sqrt{a^2 - b^2}} \left[a^2 \frac{E(k)}{K(k)} - b^2 \right] \quad (4)$$

TABLE 5: The microcrack distribution at failure of all models.

| Failure mode | Microcrack coalescence mode | Flaws parameter (co/non- α - β - D) | Microcrack distribution at failure |
|-------------------------------|---|---|---|
| Tensile failure | Tensile crack coalescence | Co-0°-0°-10 mm Co-15°-15°-10 mm Co-30°-30°-10 mm Co-45°-45°-15 mm |  |
| | Tensile crack coalescence | Non-45°-0°-10 mm Non-45°-0°-15 mm Non-45°-0°-20 mm Non-45°-15°-15 mm |  |
| Shear failure | Shear crack coalescence | Co-45°-45°-5 mm Co-45°-45°-10 mm Co-60°-60°-10 mm |  |
| | Shear crack coalescence | Non-45°-60°-10 mm Non-45°-60°-15 mm Non-45°-60°-20 mm Non-45°-90°-10 mm Non-45°-90°-15 mm |  |
| Mix tensile and shear failure | Mix tensile and shear crack coalescence | Co-45°-45°-20 mm Co-45°-45°-30 mm |  |
| | Mix tensile and shear crack coalescence | Non-45°-15°-10 mm Non-45°-30°-10 mm Non-45°-30°-15 mm Non-45°-30°-20 mm Non-45°-90°-20 mm Non-45°-120°-10 mm |  |
| Split fracture | No coalescence | Co-75°-75°-10 mm Co-90°-90°-10 mm |  |
| | No coalescence | Non-45°-15°-20 mm Non-45°-120°-15 mm Non-45°-120°-20 mm |  |

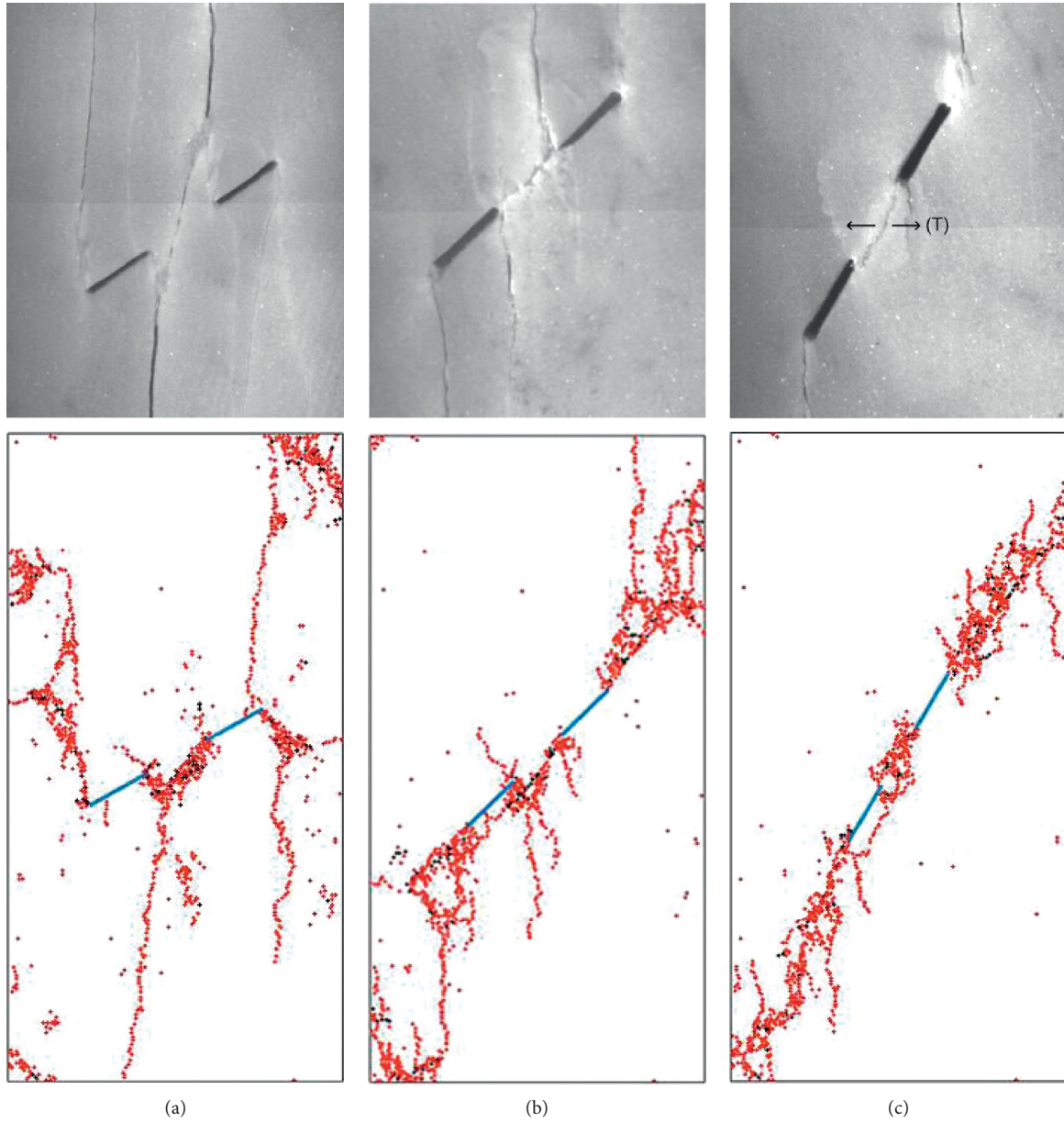


FIGURE 10: Comparison between experiment and simulation of the model with coplanar flaws with the same dip angle. (a) $\alpha = 30^\circ$. (b) $\alpha = 45^\circ$. (c) $\alpha = 60^\circ$.

The critical stress at the internal tip of the flaw is

$$\sigma(i) = \frac{2K_{II}(i) \cdot \sqrt{b(a^2 - b^2)}}{(\sin 2\alpha + 2f \cos^2 \alpha)[a^2 \cdot (E(k)/K(k)) - b^2] \cdot \sqrt{\pi}} \quad (5)$$

where $K(k)$ and $E(k)$ are the first type and second type of complete elliptic integrals.

$$\begin{cases} k^2 = 1 - \frac{b^2}{a^2}, \\ K(k) = \int_0^{\pi/2} \frac{d\varphi}{\sqrt{1 - k^2 \sin^2 \varphi}}, \\ E(k) = \int_0^{\pi/2} \sqrt{1 - k^2 \sin^2 \varphi} d\varphi. \end{cases} \quad (6)$$

Under the condition $b/a < 1$, there is always $|K_{II}(i)| < |K_{II}(o)|$, so there is always $\sigma(i) > \sigma(o)$. Therefore, the outer tip expands earlier than the inner tip, and therefore only the critical stress of the outer tip is calculated.

The relationship between the stress intensity factor of Pure I type crack and pure II type crack is as follows:

$$\frac{K_{IIc}}{K_{Ic}} \approx 1.39. \quad (7)$$

According to [29], when $K_{Ic} = 1.36 \text{ MPa} \cdot \sqrt{\text{m}}$, $K_{IIc} = 1.89 \text{ MPa} \cdot \sqrt{\text{m}}$.

For the coplanar flaws, the relationship between the critical stress and crack initiation stress with the increase in inclination angle of coplanar flaws (series 1) is shown in Figure 11. The critical stress was calculated according to

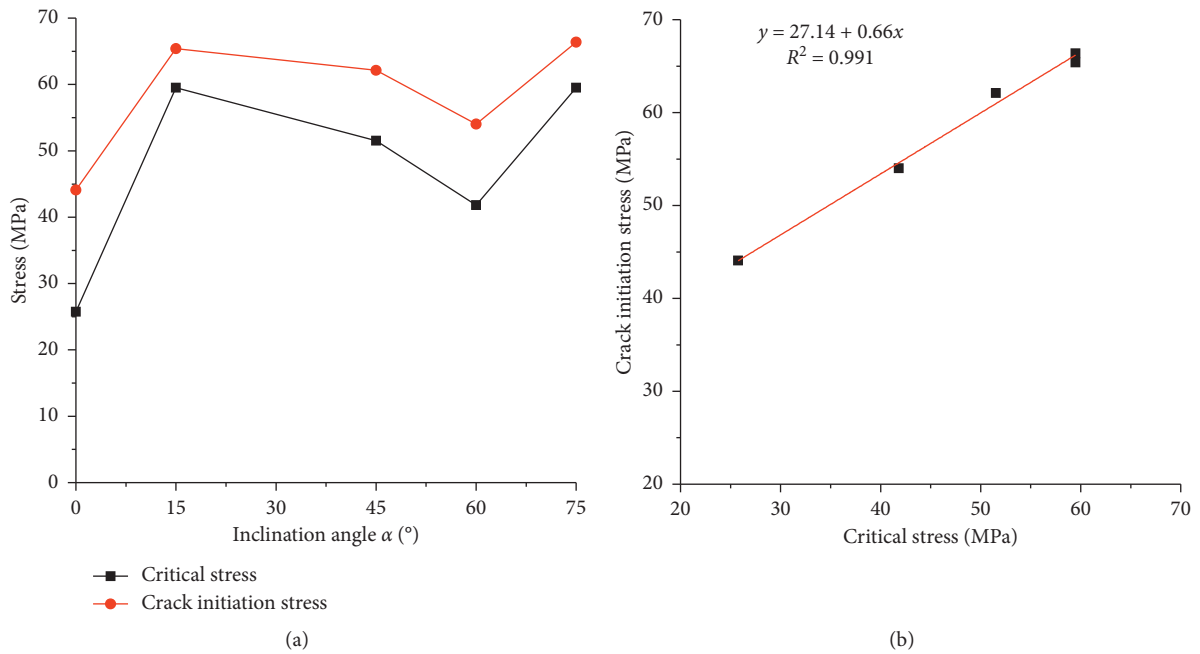


FIGURE 11: The relationship between the critical stress and crack initiation stress with increase in inclination angle of coplanar flaws (series 1).

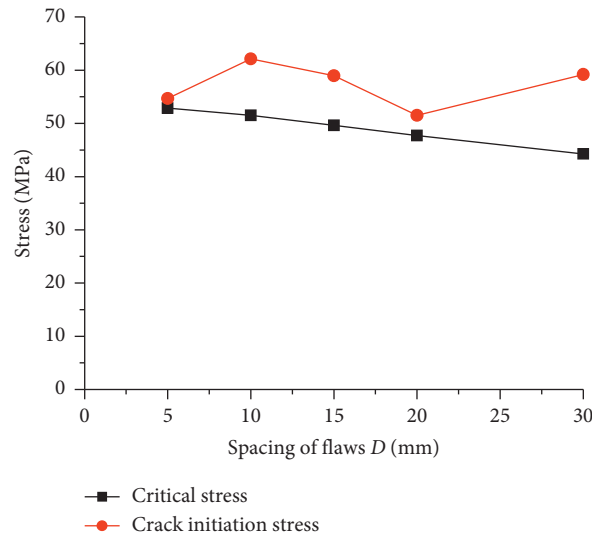


FIGURE 12: The relationship between the critical stress and crack initiation stress with increase in spacing of coplanar flaws (series 2).

formula (3), and the crack initiation stress is the same as before. Figure 11(a) shows the values of two kinds of stress; the crack initiation stress is bigger than the critical stress, but the variation tend of the two stresses is the same. The crack initiation stress is approximately 1.28 times larger than the critical stress. Figure 11(b) shows the linear fitting of the critical stress and crack initiation stress, and the correlation coefficient R^2 is equal to 0.991, which means the two kinds of stress have strong linear correlation. The physical meaning of the critical stress and the crack initiation stress is the same, but the values of crack initiation stress are bigger than the critical stress. That is because when the particle flow

simulation effects are associated with the fatigue effect of rock mass, the simulated experiment shows that, with the increase in load, the microcracks slowly extend to form a fracture zone and fracture and continue to increase until the process load fails. But, because of fatigue, stress corrosion crack, and creep, the actual bearing capacity of rock mass is lower than this value.

For the coplanar flaws, the relationship between the critical stress and crack initiation stress with increase in spacing of coplanar flaws (series 2) is shown in Figure 12. The critical stress was calculated according to formula (3), and the crack initiation stress is the same as before. Figure 12

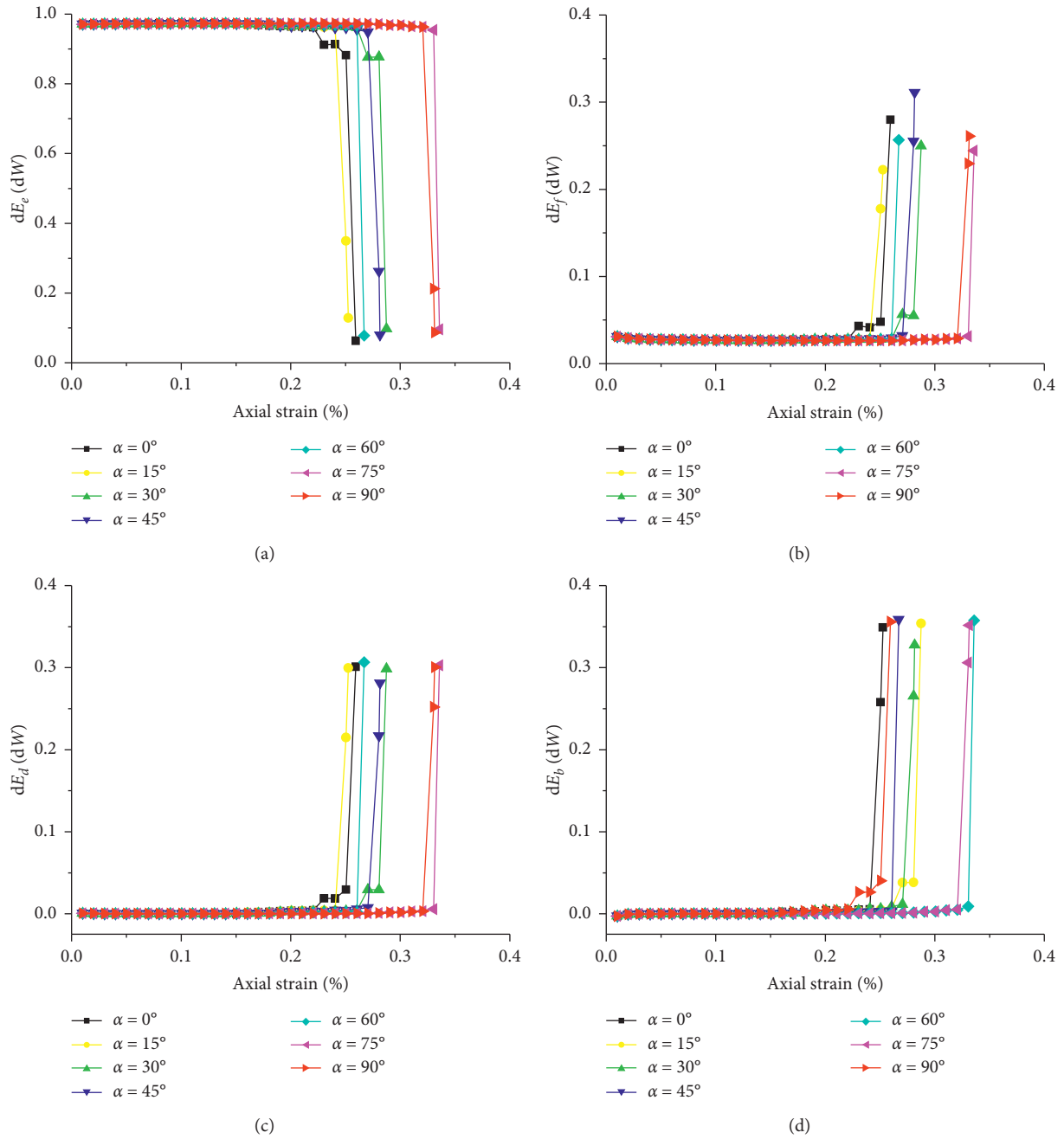


FIGURE 13: Energy dissipation laws during the model fracturing process with different dip angles (series 1).

shows the values of two kinds of stress, and the crack initiation stress is bigger than the critical stress. When the spacing of coplanar flaws is 5 mm or 20 mm, the critical stress and crack initiation stress are the closest. However, the variation trend of the two stresses is not the same, and two stress are not linearly correlated. This means that the fracture energy formula in the two coplanar flaws has some suitable conditions that require further correction.

4.2. Fracture Energy Analysis. To investigate the evolution of energy input/dissipation behaviour throughout the compression process, different energy terms are presented in an incremental form for each simulation. These energy terms include boundary work dW , body work dW_g performed by the gravity force, elastic energy dE_e stored at particle contacts upon particle deformation (containing bond strain energy dE_{pb} and strain energy dE_s), kinetic

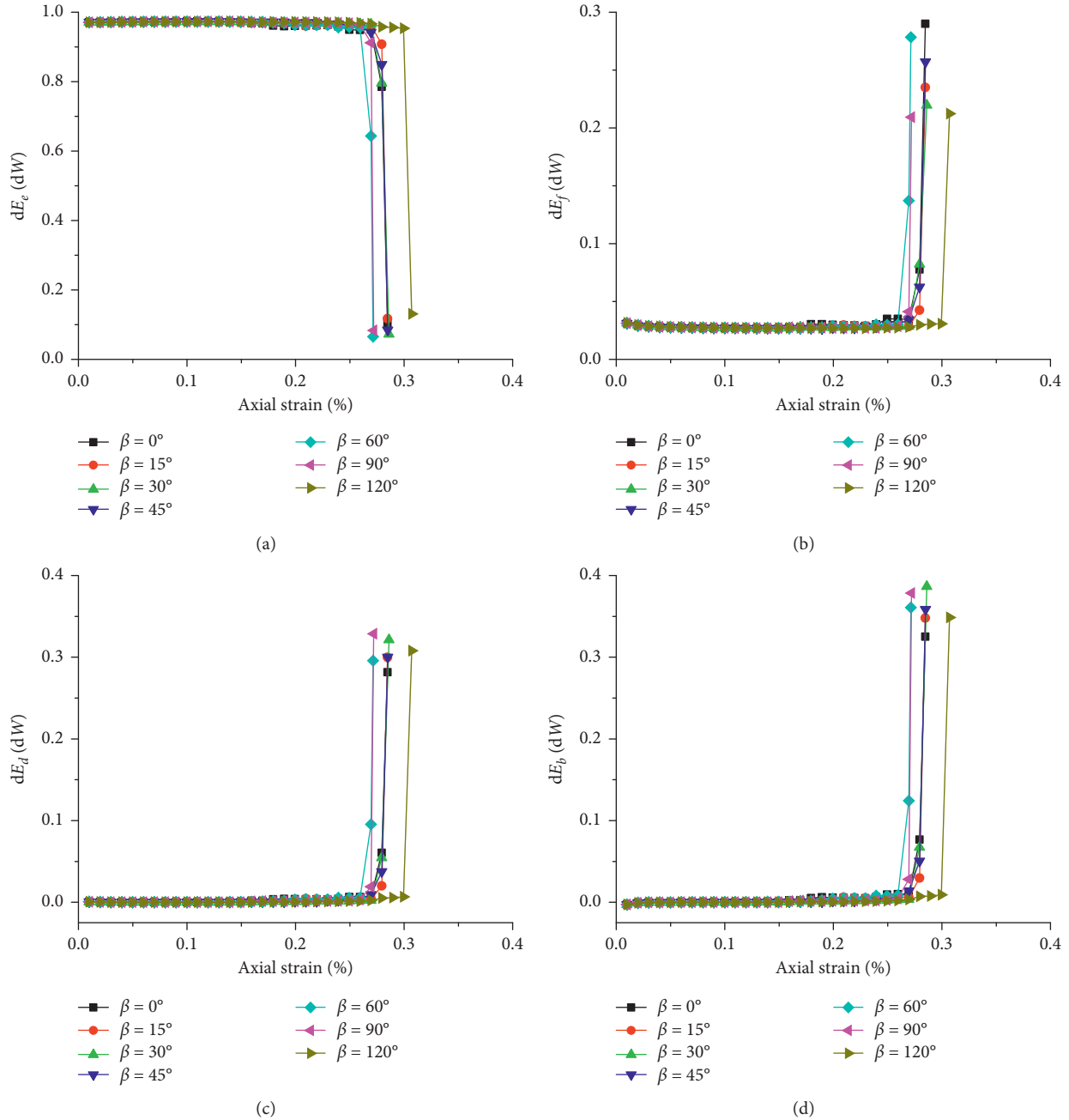


FIGURE 14: Energy dissipation laws during the model fracturing process with different step angle (series 4).

energy dE_k , interparticle friction dissipation dE_f , damping dissipation dE_d , and particle break energy dE_b by [19, 30]. In the PFC simulation, the formulae of these energies are as follows:

$$E_s = \frac{1}{2} \left(\frac{(F_n^l)^2}{k_n} + \frac{\|F_s^l\|^2}{k_s} \right), \quad (8)$$

$$E_{pb} = \frac{1}{2} \left(\frac{\bar{F}_n^2}{\bar{k}_n \bar{A}} + \frac{\|\bar{F}_s\|^2}{\bar{k}_s \bar{A}} + \frac{\bar{M}_t^2}{\bar{k}_s \bar{J}} + \frac{\|\bar{M}_b\|^2}{\bar{k}_n \bar{I}} F_s^l \right), \quad (9)$$

$$E_f := E_f - \frac{1}{2} \left((F_s^l)_o + F_s^l \right) \cdot \Delta \delta_s^u, \quad (10)$$

$$E_d := E_d - F^d \cdot (\delta \Delta t). \quad (11)$$

At any stage of compression, there is energy conservation, and the law of energy conservation gives

$$dW + dW_g = dE_e + dE_k + dE_f + dE_d + dE_b. \quad (12)$$

In the current study, body work dW_g is equal to zero, as the rock gravity was set to zero.

Due to the quasistatic loading condition, the kinetic energy of the particle set is negligible. So, format (9) can also be expressed as

$$dW = dE_e + dE_f + dE_d + dE_b. \quad (13)$$

Figure 13 recorded dE_e/dW , dE_f/dW , dE_d/dW , and dE_b/dW along with the development of axial strain in the axial strain increment of 0.1% in the model of coplanar flaws containing different inclination angles (series 1). As shown in Figure 13, the sum of four energy increment ratios is approximately equal to 1 at any time, which is consistent with the law of conservation of energy.

- (1) It can be seen from Figure 13(a), dE_e/dW stays near 0.97 in the compression process with the increase in axial strain and then rapidly reduces in the near the peak intensity. When the inclination angle is 75° and 90° , it does not form the macroscopic crack before peak strength, and the elastic energy is larger. The strengths decrease rapidly after peak strength, and the elastic energy decreases rapidly.
- (2) It can be seen from Figure 13(b), dE_f/dW stays near 0.035 in the compression process with the increase in axial strain and then rapidly increases near the peak intensity. After reaching the peak strength, the microcracks developed rapidly and the friction surface area increased, resulting in a rapid increase in friction consumption.
- (3) It can be seen from Figure 13(c), dE_d/dW stays near 0 initially with the development of axial strain, and the damping energy can increase rapidly after the model reaches the peak strength. This energy dissipation is caused by the damping force of particle motion in quasistatic loading and is also the energy dissipation part of the system.
- (4) It can be seen from Figure 13(d), dE_b/dW stays near 0 initially with the development of axial strain. The break energy increases rapidly after the model reaches the peak strength, and the break energy is greater than the particle energy and damping energy. The evolution law of dE_b/dW also explains the evolution process of particle fragmentation on the microscale, and the number of microcracks and the particle crushing energy increases. When the fracture angle is different, the energy dissipation law is basically the same, and the particle breaks when the fracture zone is formed, resulting in a sharp increase in energy consumption, and the particle breakage rate in the fracture zone is slowed down.

Figure 14 recorded dE_e/dW , dE_f/dW , dE_d/dW , and dE_b/dW along with the development of axial strain in the axial strain increment of 0.1% in the model of noncoplanar flaws containing stepped inclination angle (series 4). The four parts of energy evolution have the same rule, and the step angle has no obvious effect on the energy dissipation rule.

In general, the energy of the sample distribution mechanism from microscopic scales explains the rock particles in the process of compression fabric and fracture behaviour of evolution. The particle breakage mainly influences the stage of the small strain energy distribution difference, and the development of the entire process of compression crushing energy differs.

The flaws are common in the jointed rock mass; therefore, it is more relevant to investigate the failure mechanical behavior of rock material containing pre-existing flaws under the uniaxial compression test. The influence of dip angle, step angle, and spacing distance of two flaws on the strength and deformation of rock mass is investigated. The values of crack initiation stress and crack damage stress could contribute to the development of support measures for Jinping II Hydropower Station, and from the process of microcrack initiation, coalescence, and failure of the jointed rock mass could be judged the crack propagation and penetration in the rock mass Jinping II Hydropower Station.

5. Conclusions

The flaws are common in the jointed rock mass; therefore, it is more relevant to investigate the failure of mechanical behavior of rock material containing pre-existing flaws under the uniaxial compression test. The influence of dip angle, step angle, and spacing distance of two flaws on the strength and deformation of rock mass is investigated. The values of crack initiation stress and crack damage stress could contribute to the development of support measures for Jinping II Hydropower Station, and from the process of microcrack initiation, coalescence, and failure of the jointed rock mass could be judged the crack propagation and penetration in the rock mass Jinping II Hydropower Station. The main conclusions are as follows:

- (1) For the model with the coplanar flaws, the higher the inclination angle of coplanar flaws, the greater the peak strength of the model; and the spacing of the coplanar flaws has little effect on the peak strength. For the model with the noncoplanar flaws, when the spacing of two flaws is 10 mm, there is a rise and fall with the step angle, and when the spacing of two flaws is 15 mm or 20 mm, there is almost no change with the step angle.
- (2) In the process of stress redistribution in rock, the development of cracks can be roughly judged. As the stress increases, the microstress increases and the microcracks are appeared, and then the microstress redistributes to the next stage. Summarizing the rock bridge coalescence mode, there are four forms of rock bridge coalescences: tensile crack coalescence, shear crack coalescence, mixed tensile and shear crack coalescence, and no coalescence. Summarizing the rock failure mode, there are four forms of rock failure mode: tensile failure,

shear failure, mixed tensile and shear failure, and splitting failure.

- (3) The critical stress values and four energy ratios were obtained which use the fracture mechanics method at the different specimens. For the model with the coplanar flaws with the fixed spacing, the crack initiation stress is approximately 1.28 times larger than the critical stress, and the higher the inclination angle, the higher the particle break energy and the changing point of energy component when the microcrack grows quickly. For the model with the noncoplanar flaws with different step angles, the crack initiation stress is closest the critical stress when the spacing at 5 mm or 20 mm, the four parts of energy evolution have the same rule, and the step angle has no obvious effect on the energy dissipation rule [23].

Data Availability

The data used to support the findings of this study are available from the corresponding author upon request.

Conflicts of Interest

The authors declare that they have no conflicts of interest.

Acknowledgments

This research was supported by the National Natural Science Foundation of China (no. 51278391) and appreciated by the Itasca Consulting China Ltd.

References

- [1] M. Bahaaddini, G. Sharrock, and B. K. Hebblewhite, "Numerical investigation of the effect of joint geometrical parameters on the mechanical properties of a non-persistent jointed rock mass under uniaxial compression," *Computers and Geotechnics*, vol. 49, pp. 206–225, 2013.
- [2] A. Bobet and H. H. Einstein, "Fracture coalescence in rock-type materials under uniaxial and biaxial compression," *International Journal of Rock Mechanics and Mining Sciences*, vol. 35, no. 7, pp. 863–888, 1998.
- [3] N. Cho, C. D. Martin, and D. C. Segol, "A clumped particle model for rock," *International Journal of Rock Mechanics and Mining Sciences*, vol. 44, no. 7, pp. 997–1010, 2007.
- [4] W. Chu, "The stability and structural safety assessment of tunnel surrounding rock under buried deep conditions," Postdoctoral Report, 2009.
- [5] D. Huang, J. Wang, and L. Su, "Comprehensive study on the smooth joint model in DEM simulation of jointed rock mass," *Granular Matter*, no. 17, pp. 775–791, 2015.
- [6] D. Huang and X. Li, "Numerical simulation research on characteristic strength of marble based on development of microcrack," *Rock and Soil Mechanics*, vol. 38, no. 1, pp. 253–262, 2017.
- [7] F. Erdogan, "On the stress distribution in plates with collinear cuts under arbitrary load," in *Proceedings of the fourth U.S. National Congress of Applied Mechanics*, vol. 1, pp. 547–553, Berkeley, CA, USA, June 1962.
- [8] K. Esmaili, J. Hadjigeorgiou, and M. Grenon, "Estimating geometrical and mechanical REV based on synthetic rock mass models at Brunswick mine," *International Journal of Rock Mechanics and Mining Sciences*, vol. 47, no. 6, pp. 915–926, 2010.
- [9] J. F. Hazzard and R. P. Young, "Simulating acoustic emissions in bonded-particle models of rock," *International Journal of Rock Mechanics and Mining Sciences*, vol. 37, no. 5, pp. 867–872, 2000.
- [10] Y.-P. Li, L.-Z. Chen, and Y.-H. Wang, "Experimental research on pre-cracked marble under compression," *International Journal of Solids and Structures*, vol. 42, no. 9-10, pp. 2505–2516, 2005.
- [11] A. R. Martinez, "Fracture coalescence in natural rock," M.Sc. thesis, Massachusetts Institute of Technology, Cambridge, MA, USA, 1999.
- [12] D. Mas Ivars, M. Pierce, C. Darcel et al., "The synthetic rock mass approach for jointed rock mass modeling," *International Journal of Rock Mechanics and Mining Sciences*, vol. 48, no. 2, pp. 219–244, 2011.
- [13] J. W. Park and J. J. Song, "Numerical simulation of a direct shear test on a rock joint using a bonded-particle model," *International Journal of Rock Mechanics and Mining Sciences*, vol. 46, no. 8, pp. 1315–1328, 2009.
- [14] D. O. Potyondy and P. A. Cundall, "A bonded-particle model for rock," *International Journal of Rock Mechanics and Mining Sciences*, vol. 41, no. 8, pp. 1329–1364, 2004.
- [15] M. Pierce, D. Mas Ivars, P. Cundall, and D. Potyondy, "A synthetic rock mass model for jointed rock," in *Rock Mechanics: Meeting Society's Challenges and Demands*, E. Eberhardt, Ed., pp. 341–349, Taylor & Francis, London, UK, 2007.
- [16] C. H. Park and A. Bobet, "Crack coalescence in specimens with open and closed flaws: a comparison," *International Journal of Rock Mechanics and Mining Sciences*, vol. 46, no. 5, pp. 819–829, 2009.
- [17] C. H. Park and A. Bobet, "Crack initiation, propagation and coalescence from frictional flaws in uniaxial compression," *Engineering Fracture Mechanics*, vol. 77, no. 14, pp. 2727–2748, 2010.
- [18] M. Sagong and A. Bobet, "Coalescence of multiple flaws in a rock-model material in uniaxial compression," *International Journal of Rock Mechanics and Mining Sciences*, vol. 39, no. 2, pp. 229–241, 2002.
- [19] J. Wang and H. Yan, "On the role of particle breakage in the shear failure behavior of granular soils by DEM," *International Journal for Numerical and Analytical Methods in Geomechanics*, vol. 37, no. 8, pp. 832–854, 2011.
- [20] L. N. Y. Wong and H. H. Einstein, "Crack coalescence in molded gypsum and Carrara marble: part 1. macroscopic observations and interpretation," *Rock Mechanics and Rock Engineering*, vol. 42, no. 3, pp. 475–511, 2009.
- [21] L. N. Y. Wong and H. H. Einstein, "Crack coalescence in molded gypsum and Carrara marble: part 2-microscopic observations and interpretation," *Rock Mechanics and Rock Engineering*, vol. 42, no. 3, pp. 513–545, 2009.
- [22] L. N. Y. Wong and H. H. Einstein, "Systematic evaluation of cracking behavior in specimens containing single flaws under uniaxial compression," *International Journal of Rock Mechanics and Mining Sciences*, vol. 46, no. 2, pp. 239–249, 2009.
- [23] R. H. C. Wong and K. T. Chau, "Crack coalescence in a rock-like material containing two cracks," *International Journal of Rock Mechanics and Mining Sciences*, vol. 35, no. 2, pp. 147–164, 1998.

- [24] L. N. Y. Wong, *Crack coalescence in molded gypsum and Carrara marble*, Ph.D. thesis, Massachusetts Institute of Technology, Cambridge, UK, 2008.
- [25] S.-Q. Yang and H.-W. Jing, "Strength failure and crack coalescence behavior of brittle sandstone samples containing a single fissure under uniaxial compression," *International Journal of Fracture*, vol. 168, no. 2, pp. 227–250, 2011.
- [26] S.-Q. Yang, Y.-H. Huang, H.-W. Jing, and X.-R. Liu, "Discrete element modeling on fracture coalescence behavior of red sandstone containing two unparallel fissures under uniaxial compression," *Engineering Geology*, vol. 178, pp. 28–48, 2014.
- [27] X.-P. Zhang and L. N. Y. Wong, "Cracking processes in rock-like material containing a single flaw under uniaxial compression: a numerical study based on parallel bonded-particle model approach," *Rock Mechanics and Rock Engineering*, vol. 45, no. 5, pp. 711–737, 2012.
- [28] X.-P. Zhang and L. N. Y. Wong, "Loading rate effects on cracking behavior of flaw-contained specimens under uniaxial compression," *International Journal of Fracture*, vol. 180, no. 1, pp. 93–110, 2013.
- [29] S. Zhang and Q. Z. Wang, "Determination of marble fracture toughness by using variable crack one size specimens," *Engineering Mechanics*, vol. 24, no. 6, pp. 31–35, 2007.
- [30] B. Zhou, J. Wang, and H. Wang, "A new probabilistic approach for predicting particle crushing in one-dimensional compression of granular soil," *Soils and Foundations*, vol. 54, no. 4, pp. 833–844, 2014.